

https://doi.org/10.1038/s44172-024-00259-4

An experimental system for detection and localization of hemorrhage using ultrawideband microwaves with deep learning

Check for updates

Eisa Hedayati [⊕] ^{1,2,5}, Fatemeh Safari ^{1,2,5}, George Verghese ^{1,2}, Vito R. Ciancia³, Daniel K. Sodickson ^{1,2}, Seena Dehkharghani [⊕] ^{1,2,4,6} ⊗ & Leeor Alon [⊕] ^{1,2,6} ⊗

Stroke is a leading cause of mortality and disability. Emergent diagnosis and intervention are critical, and predicated upon initial brain imaging; however, existing clinical imaging modalities are generally costly, immobile, and demand highly specialized operation and interpretation. Low-energy microwaves have been explored as a low-cost, small form factor, fast, and safe probe for tissue dielectric properties measurements, with both imaging and diagnostic potential. Nevertheless, challenges inherent to microwave reconstruction have impeded progress, hence conduction of microwave imaging remains an elusive scientific aim. Herein, we introduce a dedicated experimental framework comprising a robotic navigation system to translate blood-mimicking phantoms within a human head model. An 8-element ultra-wideband array of modified antipodal Vivaldi antennas was developed and driven by a two-port vector network analyzer spanning 0.6–9.0 GHz at an operating power of 1 mW. Complex scattering parameters were measured, and dielectric signatures of hemorrhage were learned using a dedicated deep neural network for prediction of hemorrhage classes and localization. An overall sensitivity and specificity for detection >0.99 was observed, with Rayleigh mean localization error of 1.65 mm. The study establishes the feasibility of a robust experimental model and deep learning solution for ultra-wideband microwave stroke detection.

Despite recent progress, stroke remains a leading cause of death and disability, disproportionately affecting low-income countries and the economically disadvantaged^{1,2}. In the US alone, ~795,000 individuals are affected per annum, with 1 in every 4 people suffering a stroke in their lifetime³. It is estimated that ~1.9 million neurons are lost each minute during a stroke⁴; however, intravenous tissue plasminogen activator—the only thrombolytic therapy approved by the U.S. Food and Drug Administration—is successfully administered in only ~10% of patients due to strict guidelines prohibiting its use 4.5 h beyond a stroke event or in patients with hemorrhage. The resulting economic burden of stroke is thus staggering, with 34% of global total healthcare expenditure attributed to stroke, and >USD 56 billion in associated costs in the U.S. alone. Urgent diagnosis and intervention are therefore central pillars of contemporary management guidelines, with initial triage of stroke patients hinging first upon exclusion of brain hemorrhage by advanced neuroimaging5-8.

Existing imaging solutions comprise primarily magnetic resonance imaging (MRI)8-10 and computed tomography (CT)11-16 which, while wellestablished, present numerous drawbacks including: (1) lack of portability for deployment to preclinical settings, engendering critical treatment delays until hospital arrival in most cases 17,18; (2) high costs, exceeding millions of dollars for contemporary clinical CT and MR systems, proving prohibitive in many environments and perpetuating immense imbalances in global health¹⁹. Specifically, with two-thirds of the global population lacking accessible medical imaging, RAD-AID estimates that 3-4 billion excess deaths could be averted through improved access²⁰; (3) lengthy scan and protocol durations imparting additional delays that further reduce the likelihood of favorable clinical outcomes^{4,12,13,21}; (4) requisite levels of specialization necessary for operation and interpretation of such examinations^{22,23}; and, (5) safety concerns relating to ionizing radiation in CT and strong magnetic fields in MRI¹³. While the recent introduction of CT scanners in specialized mobile stroke ambulance units²⁴ may alleviate

¹Center for Advanced Imaging Innovation and Research (CAI2R), New Yorsity School of Medicine, New York, NY, USA. ²Center for Biomedical Imaging, New York University School of Medicine, New York, NY, USA. ³LaGuardia Studios, New York University, New York, NY, USA. ⁴Department of Neurology, New York University Langone Medical Center, New York, NY, USA. ⁵These authors contributed equally: Eisa Hedayati, Fatemeh Safari. ⁶These authors jointly supervised this work: Seena Dehkharghani, Leeor Alon. ⊠e-mail: Seena.Dehkharghani@nyulangone.Org; Leeor.Alon@nyulangone.Org

some delays, their operational costs have remained untenably high for all but a small number of urban centers worldwide^{25–27}. The demand for cost-effective, fast, safe, and deployable small-form diagnostic instruments is thus unmet, motivating new directions using sensors.

The use of low-energy microwaves as a probe of tissue dielectric properties has been explored and represents an intriguing means of characterizing tissue properties^{28–31}. Several potential advantages over MRI and CT have motivated the development of such microwave imaging (MWI) systems, including: (1) extremely low operational power and lack of ionizing radiation, enabling biologically harmless use unhindered by indwelling implants and ferromagnetic objects; (2) remarkably high acquisition speeds; (3) low production cost; and (4) small form factor^{32–37}. Given these advantages, in recent years, a growing number of commercial companies have implemented microwave solutions for detection stroke as well as other of diseases^{38–41}.

The characterization of biologic tissues using microwave radiation entails the collection of scattering (S)-parameters, based in transmission and reflection measurements, commonly achieved using vector network analyzers (VNA)42 or with software defined radio (SDR) to drive radiation of a high directivity antenna⁴³. Most existing MWI systems obtain measurements in the low (e.g., 0.5-2.0) GHz range, owing in part to the relative ease of corresponding antenna design and fabrication³⁰. With early studies casting doubt upon any additional benefits from higher forbidden frequencies²⁹ (due to exponential penetration losses from electromagnetic skin effects and tissue mismatch) as well as a generalized reduction in dielectric contrast beyond 5 GHz, low frequency MWI has remained the favored strategy⁴⁴. Nevertheless, rigorous experimental investigation into ultra-wideband (UWB) systems is still lacking, and the potential benefits afforded by their greater resolving ability and sensitivity to superficial processes remains unknown 45,46. The emergence of contemporary machine learning algorithms for reconstruction has further advanced the potential of microwave systems, such as for classification and localization for stroke^{28,30,47,48}; however, it bears emphasis that past approaches to hemorrhage detection have generally been limited to models of intraparenchymal hematomas (IPH), a subclass of well-circumscribed bleeding mostly confined to the parenchymal substrate of the brain; meanwhile, more complex models recapitulating catastrophic, superficial subarachnoid hemorrhage (SAH) and other diffuse extracerebral bleeding has lagged^{28,30,47,48}, pointing to vast potential applications for systems leveraging high frequency capabilities.

We have previously shown the potential for such UWB (0.5–6.0 GHz) systems through in silico simulation and using a deep neural network for classification and localization of intracranial hemorrhage, exhibiting excellent classification (AUC 0.996) and localization (sub-millimeter error) accuracy across varied anatomical human head geometries and noise conditions³¹. However, translation from in silico environments to fully realized, physical UWB systems demands non-trivial hardware and software solutions dedicated to the specific experimental objective. In this study, we describe the conception, design, and development of a system for UWB microwave experimentation, benchtop hypothesis testing, analysis, and hardware prototyping for prediction of brain hemorrhage. A custom UWB system was engineered for operation up to 9.0 GHz and paired with a human head model to test morphologically variable hemorrhages under remote robotic control. The system was used to train a dedicated artificial neural net, hypothesizing robust and frequency-dependent hemorrhage localization, and classification accuracy benefitting from UWB interrogation.

Methods Antenna design

UWB microwave transmission and reception in the near field was accomplished with custom, circularly-loaded antipodal Vivaldi antennas modified from Siddiqui J. et al. having shown desirable directive properties for this antenna structure⁴⁹. Initial simulations were conducted using the HFSS simulation environment (Ansys Inc., Canonsburg, PA, USA), where the

conductor dimensions were modified to support efficient operation (S11 < $-10~\mathrm{dB}$) at frequencies between 0.75 and 10 GHz. Upon arriving at the desired parameters, the antenna dimensions were 125.3 mm \times 85.4 mm \times 1.524 mm (length x width x thickness). The antenna was fabricated on a Rogers RO4003C substrate with a dielectric constant of 3.55 and an SMA connector was soldered to the antenna structure. Overall, a total of eight antennas were positioned in a ring, encircling a head phantom in a common XY-plane as illustrated in Fig. 1a.

Phantom design and general setup

A human head phantom was designed, and 3D printed, based on the SAM head phantom 50 . The head model comprised a superficial (radially) outer compartment mimicking muscle and an inner compartment of *average* brain tissue, with outer dimensions of 258 mm (height) x 175 mm (width) x 122 mm (depth) and an inner compartment with dimensions of 199 mm \times 145 mm x 92 mm (Supplementary Fig. 1, Supplemental Results). The phantom was printed using a stereolithography 3D printer, (Phrozen Mega Sonic 8 K, Phrozen Tech Co Ltd., Taiwan) leaving an aperture at its crown such that blood phantoms of varying size and morphology could be introduced to the inner compartment and navigated remotely under robotic guidance as detailed below.

Five different hemorrhage models, each simulating the dielectric properties of intracranial hemorrhage, were designed in order to introduce

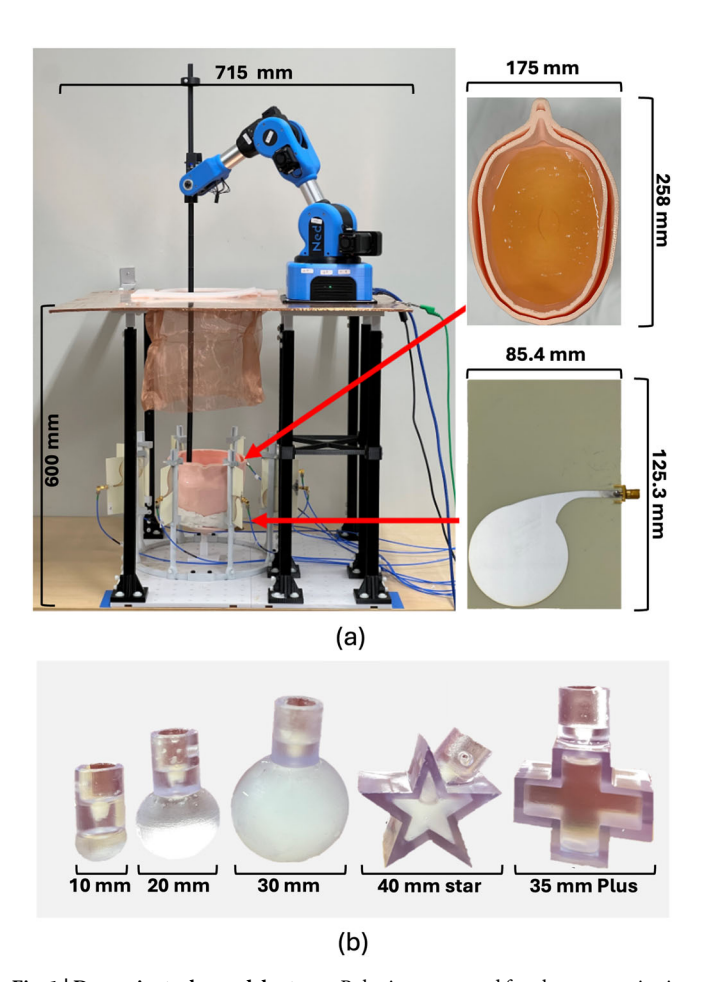


Fig. 1 | **Dynamic stroke model setup. a** Robotic system used for phantom navigation within the head model. A 650 mm rod was used to connect the robot to the blood phantom (left). A three-dimensional printed head model was used and filled with brain-mimicking dielectric liquid (top-right, with its position in the model shown by paired red arrows) and encircled by an array of custom ultra-wideband antipodal-Vivaldi antennas for near-field measurements (bottom-right). **b** Three-dimension printed blood phantoms including spherical hemorrhage models of varying inner diameter, as well as morphologically more complex star- and plus-shaped models.

dielectric disturbances within the head, including: i. three distinct spherical models with diameters of 10 mm, 20 mm, and 30 mm (with inner volumes of 0.52 ml, 4.18 ml, and 14.14 ml, respectively); ii. A star-shaped model; (3.7 ml); and iii. a plus-shaped model (9.5 ml), each used to introduce complex dielectric disturbances to the head phantom during dedicated experimentation. The blood phantoms were designed as fillable volume shells with single compartment and fabricated using the Formlabs Form 3B (Formlabs Inc., Massachusetts, USA) SLA 3D printer using the transparent biomed clear resin. The blood, muscle, and brain materials were compositions of tween 20 (polysorbate 20), NaCl, and water to reflect dielectric properties of the corresponding tissue. Utilization of liquids was particularly important for the brain compartment as the goal for this dynamic phantom was to move a second blood compartment within the head and this required. Further details on the composition of the liquids can be found in the Dielectric Liquid Preparation section within the Supplemental Materials. The head phantom, blood phantom and positioning table are illustrated in Fig. 1a, b.

Mechanical and robotic localization system

To ensure fixation of the antennas relative to the head phantom, a 3D printed positioning table was designed with holders in order to immobilize the antenna array. A system of self-locking tiles was 3D printed and interlocked to meet the specifications of the phantom but readily modifiable to accommodate a wide range of experimental layouts. On the reverse face of each tile, recesses were engineered to house nuts and to provide a robust base for secure bolt fixation. Custom-designed tile holders were produced for the head phantom and antennas, and the overall configuration was designed in order to maximize stability of the phantom and antenna array during experimentation.

To ensure precise navigation, a Niryo Ned (Niryo robotique industrielle, Wambrechies, France) robotic system was used, providing a repeatability of 0.5 mm⁵¹. The system was equipped with self-reporting feedback on the spatial coordinates of the hemorrhage model in real time. In order to permit navigation of the phantom within the head model under robotic guidance, a firm linear rod of length 650 mm was 3D printed from Acrylonitrile Butadiene Styrene (ABS) having a dielectric constant of ~3.2 used to articulate the hemorrhage to the robotic arm⁵². To mitigate coupling between the robot and the antenna array, the robot was elevated and placed on a grounded copper sheet with an encircling copper mesh around the opening through which the rod entered. Custom software was developed in Python for design of the automation protocol and execution of the trajectory (Fig. 1a).

Acquisition procedure

A 2-port vector network analyzer (VNA) system (ZNB-20, Rohde & Schwarz GmbH, Munich, Germany) was used to support UWB measurements and was coupled to a switch matrix (ZN-Z84, Rohde & Schwarz GmbH, Munich, Germany) to expand the number of measurable ports to eight channels. This arrangement allowed computation of a full 8-port Sparameter network, allowing comprehensive characterization of transmission and reflection properties. The range of measurement spanned from 0.6-9.0 GHz, with a total 8412 frequencies in stepped sweep mode, with 1 MHz steps. While the antenna had a reflection coefficient of -10 dB at 0.75 GHz, a lower minimum frequency of 0.6 GHz was chosen as the lower bound of the measurement sweep in order to assess for potentially valuable information content from the lower frequencies (despite the declining antenna efficiency at those frequencies, where reflection coefficients were <~ −3 dB). An n-port Unknown through—Open—Short—Match (UOSM) calibration 42,53-55 was performed at the ends of the 8 coaxial cables to improve data quality and measurement accuracy⁵⁵.

For each acquisition, the robotic navigation system was used to translate the position of the hemorrhage phantom within the inner brain compartment of the phantom. After each translation, S-parameter measurements were conducted using the VNA and switch matrix to toggle through the antenna array before advancing the hemorrhage to its subsequent location. Importantly, when utilizing the robot in conjunction with

the rod, boundaries arising from the inner wall of the head impeded the extent of translation in some dimensions, dependent upon the geometry of each hemorrhage phantom; consequently, the trajectory of the phantoms was prescribed specifically such that the peripheral-most station was made uniform and could accommodate every one of the hemorrhage phantoms without perturbing the head. We established a grid with intervals of 10 mm in the X-, Y-, and Z-directions; bounding box dimensions for the largest hemorrhage were 90 mm, 95 mm, and 60 mm, respectively. This resulted in a total of 127 positions within the head phantom, each of which was used in the random navigation trajectory of the robot-rod-phantom assembly.

Measurements for the brain and muscle-, air-, and water-filled head phantom substrates (motivation for utilization of these measurements can be found in the Neural network training and validation), were conducted with the rod placed in different positions of the phantom, however, without the blood mimicking stroke phantoms attached to the end of the rod. These measurements were conducted to ensure that model training was unbiased by the presence of the rod itself. To address the risk of overfitting, which is well-recognized in machine learning algorithms trained on limited data, we conducted additional measurements with the head phantom filled by air or water rather than hemorrhage as a means of data augmentation.

Software was developed in Python to interface with the VNA and robot using vendor-provided libraries in order to automate data acquisition. The complex-valued S-parameters were processed using the open-source scikitrf library⁵⁶. A front-end interface was developed using PySide6 libraries providing real-time plotting of the scattering measurements, robot movements, and tracking of captured data. A desktop PC was used to interface to the VNA using a USB port and to the robot over Ethernet cable. All final acquisitions were performed with the head phantom filled with human brain-mimicking (interior compartment) and muscle-mimicking (exterior compartment) liquids for the five different hemorrhage phantoms, note that these acquisitions were repeated once for air-filled (empty) head phantom and another time for water-filled head phantom as well. The acquisition time for each point when using a 100 kHz Intermediate Frequency (IF) bandwidth was 72 s, with a 12 s delay (measured empirically) imposed after each translation to mitigate motion-related noise.

Neural network architecture

The neural network architecture proposed in this study was tailored to interpret complex S-parameter data. The architecture was segmented into two cardinal components: the convolutional layers and the terminal fully connected segments (Fig. 2). The former is characterized by a Residual ConvBot (Fig. 2a) and a series of bottleneck residual blocks⁵⁷ (Fig. 2b), termed "ResidualBlocks". These ResidualBlocks function as feature extractors, converting intricate, high-dimensional data into lowerdimensional form while retaining important information. The unique arrangement of these ResidualBlocks ensured a balance between model intricacy and operational output. The terminal components of the network were anchored by a series of fully connected layers. A linear layer served as an integration point for the outputs of the ConvBots (Fig. 2c), combining the magnitude and phase (derived from real and imaginary components) of the input data. The layers were designed for discrete predictive functions, including pinpointing the location coordinates of the hemorrhage and classifying the hemorrhage shape. Full details of the network architecture can be found in the Neural Network Architecture section in the Supplemental Materials.

Neural network training and validation

The network included three outputs comprising two classifications (multiclass classification with SoftMax) and a three-dimensional regression. Multi-task learning network training was performed with the Adam optimizer⁵⁸ using the following loss function:

$$loss = \frac{(1 - \alpha)}{N} \sum (L_1 + MSE + dist(p, \hat{p})) + CE_1 + CE_2$$
 (1)

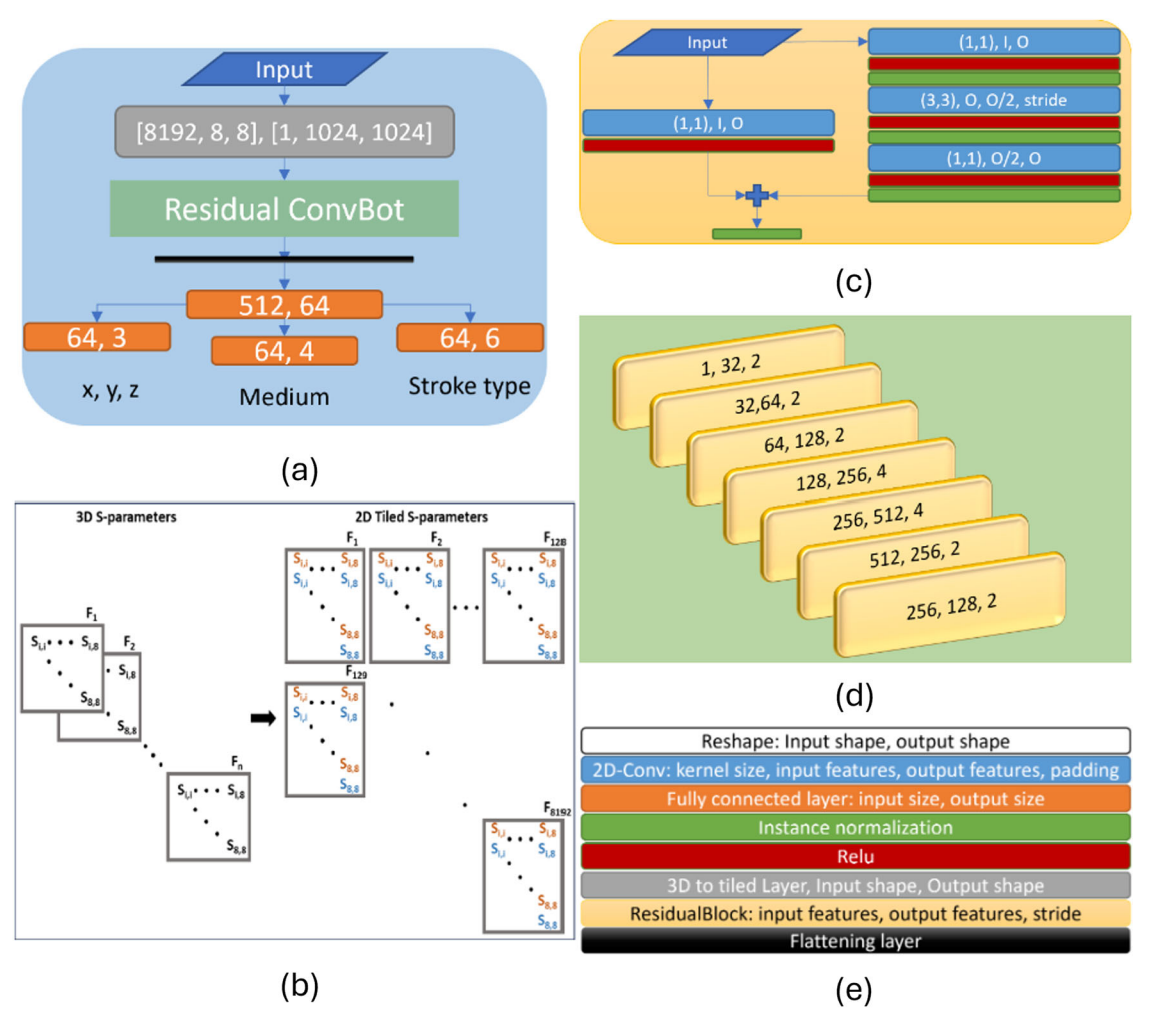


Fig. 2 | Network architecture. a The RobotNet structure with (b) a tiling layer for preprocessing of data. c Seven Residual Blocks were used as building blocks for the Residual ConvBot (d) design. The architecture contains several fully connected layers for the final output prediction. e dictionary illustrating the layer structure.

$$\alpha = \begin{cases} 0 & \text{hemorrhage} \\ 1 & \text{no hemorrhage} \end{cases}$$

where p is the ground truth location and \hat{p} is the predicted location. L_1 , MSE, and dist are the 1-norm, mean squared error, and distance difference between ground truth and predicted locations, respectively. N denotes the batch number, CE denotes the cross-entropy loss, and α ensures that the gradients for localization become zero in those cases for which the hemorrhage did not exist (i.e., no-hemorrhage class), while still allowing training for the classification task. The initialization of the learning rate of the Adam optimizer was set to 0.0001, which was decreased every hundred epochs by a factor of $\frac{1}{10}$. The network was trained on all media for 500 epochs with batch sizes of 48 over 70% of the data and tested on the remaining 30% of data of only the brain-filled head phantom excluding the air- and water-filled. The air- and water-filled phantom datapoints were used for augmentation during training to reduce potential overfitting but were not used in the test set.

From the training set, 10% of the dataset was held out for validation and hyper-parameter optimization. The hold-out method was used for data separation in all stages. To have a fair comparison, 30% of the dataset was randomly chosen from the initial 127 locations. Of the chosen test locations, all the related measurements were excluded from training and validation sets. This ensured the network remained blinded to these entries thus eliminating cross-contamination between training and test sets.

Evaluation of frequency range and antenna number

An ablation study was conducted to investigate the effects of varying the frequency range and number of antennas on network performance. Consistency in all other hyperparameters was maintained to isolate the impact of the selected variables. For the frequency range evaluation, four distinct spans were chosen: 0.6-1.5 GHz, 0.6-3 GHz, 0.6-6 GHz, and the full range of 0.6-9 GHz. For each span, we adapted the S-parameter matrix to correspond to the chosen frequency band by retaining the pertinent rows and columns and setting others to zero before network training commenced. After zeroing out the undesired frequencies, classification and localization errors were evaluated. For the evaluation of the number of antennas used on network performance, the following combinations of antennas were tested: (i) antennas 1 and 3; (ii) antennas 1, 3, and 5; (iii) antennas 0, 1, 4, and 5; and iv. all 8 antennas in the array. As with the exploration of frequency dependency, the S-parameter matrix was modified for each configuration, with relevant rows and columns preserved and non-pertinent ones nullified before network training.

Statistical analysis

Network performance was summarized with a confusion matrix for multiclass classification using frequency spans of 0.6–1.5 GHz, 0.6–3.0 GHz, 0.6–6.0 GHz, and 0.6–9.0 GHz. The specificity and sensitivity of hemorrhage detection was computed. To assess the fidelity of the localization predictions, the probability distribution function (PDF) of the error in x-and y-directions, XY-plane, and XYZ-space were computed and plotted for frequency spans of 0.6–1.5 GHz, 0.6–3 GHz, 0.6–6 GHz, and 0.6–9 GHz.

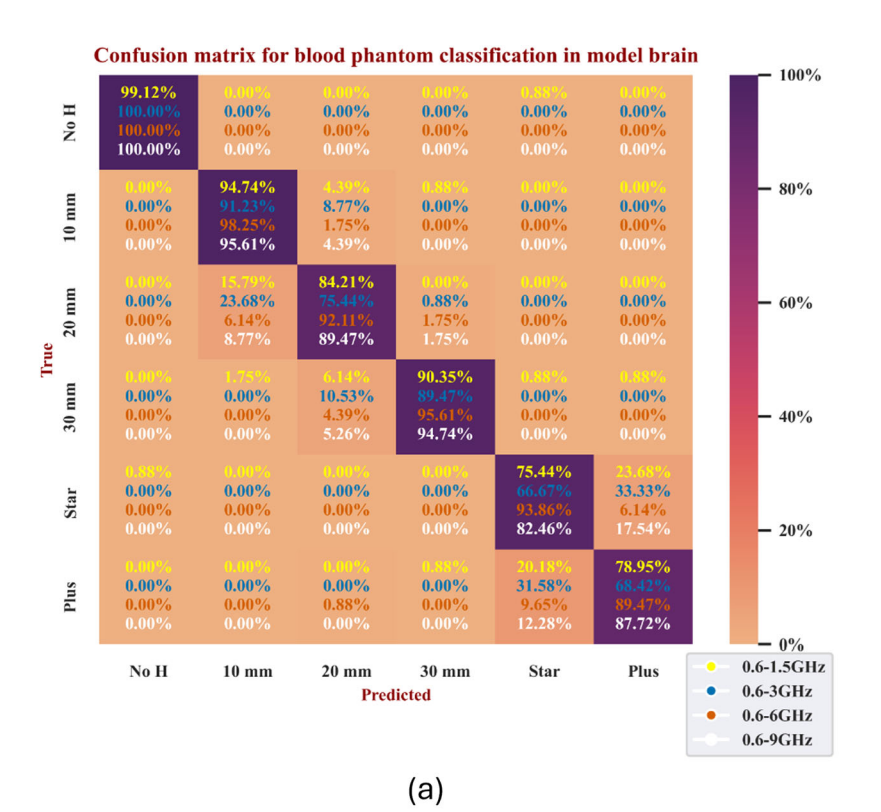
Distance error in hemorrhage localization was expressed in a normalized histogram of the distance error, with the single variate (X- and Y-directions) data fitted to a folded normal distribution function⁵⁹, and the bi-variate (in XY-plane) distance errors fitted to a Rayleigh distribution function⁶⁰. Notably, because an array of distributed channels did not exist in the z-direction, a declining accuracy was anticipated in z-direction, which was confirmed in preliminary analysis. All statistical analysis was performed using the SciPy⁶¹ library in python.

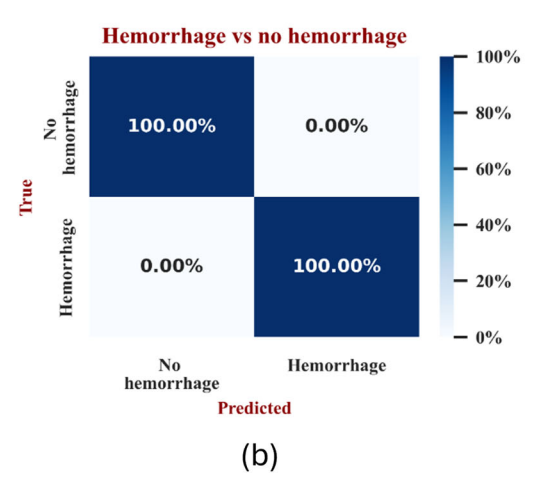
Results

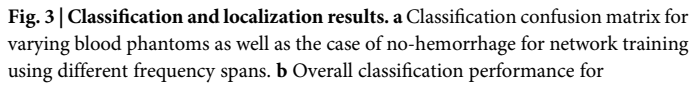
Excellent performance was demonstrated using the complete antenna array together with the entire range of UWB frequencies. Specifically, sensitivity and specificity of >0.99 were observed for hemorrhage detection, with an overall median localization error of 1.67 mm. Full results for classification and localization tasks are summarized in Fig. 3. Specifically, the larger frequency spans, of 0.6–6.0 GHz and 0.6–9.0 GHz, outperformed the narrower

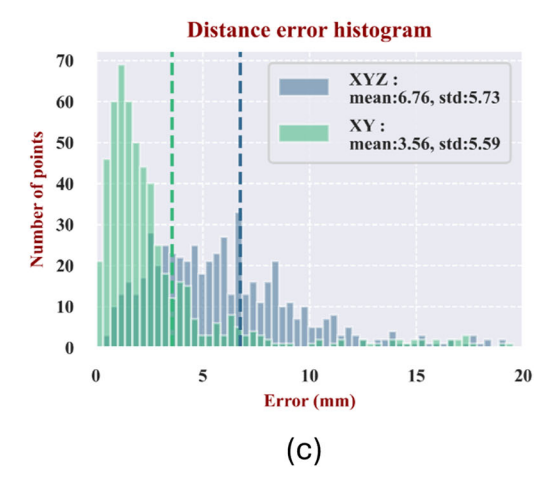
ranges in classification, Notably, despite excellent overall performance in the multi-class classification task for the 0.6–6.0 GHz range, there were a small number of instances for which a plus-shaped phantom was misclassified as a 20 mm diameter sphere, while the full frequency range exhibited better performance in discriminating spherical and non-spherical phantoms. Together, the results suggest that the extended UWB frequency ranges generally provide a superior combination of localization (with a median distance error of 1.67 mm in the xy-plane, Table 1) and classification performance (Fig. 3).

Among the individual sub-ranges of frequencies, the 0.6–6.0 GHz span yielded the best overall performance in classification of hemorrhage classes, peaking in its identification of the smallest (10 mm diameter) spherical phantom at a classification accuracy of 98.25% and a misclassification rate of only 1.75%. Overall multi-class classification for this frequency span was 94.88%. The lowest individual performance was 81.87% for the frequency span 0.6–3.0 GHz. Importantly, there was high overall sensitivity to the









hemorrhage (all phantoms combined) versus no hemorrhage, demonstrating overall sensitivity and specificity of >0.99. c Histogram of the localization error in the XYZ-space and XY-plane.

morphological characteristics of the hemorrhage phantoms; specifically, using the full frequency rage (0.6–9.0 GHz) there were no instances of a spherical phantom of any size being misclassified as a non-spherical phantom, or vice-versa. Further, a strong capacity for discrimination of varying spherical phantom volumes was observed, with no cases of the smallest 10 mm sphere being misclassified as the largest 30 mm sphere, or vice-versa. Only a small percentage (10.53%) of hemorrhages in the 20 mm class were misclassified as either a 10 mm or 30 mm hemorrhage. The single worst performing classification task was observed in prediction of the star-shaped phantom using the 0.6-3.0 GHz sub-range, for which 33.33% of cases were misclassified as plus-shaped phantoms; however, only 6.14% of such cases were misclassified using the frequency sub-range of 0.6–6 GHz (Fig. 3a).

Table 1 | Median Error for different frequency spans

Frequency span (GHz)	Median error (mm)						
	X	Υ	Z	XY	XYZ		
0.6–1.5	2.52	1.67	3.93	3.82	6.61		
0.6–3	1.13	1.04	4.46	1.9	5.68		
0.6–6	1.03	0.99	5.66	1.69	6.79		
0.6–9	1.08	0.96	5.54	1.67	6.85		
1.5–3	1.17	1.17	5.02	1.99	6.44		
3–6	1.19	1.22	6.47	2.02	7.82		
3–9	1.35	1.32	6.17	2.37	7.33		
6–9	2.38	2.05	8.89	3.96	10.95		

For the star-shaped phantom, although the volume was 3.7 ml (volumetrically almost identical to the 3.5 ml of the middle-sized sphere), excellent discrimination (>99.9%) was present between the two, further suggesting sensitivity to morphologic characteristics irrespective of volumes. The largest class-wise false-positive and false-negative rates between the star-shaped phantom and the plus-shaped phantom were 9.65% and 6.14% (star-shaped predictions), respectively, for the best performing network. The histogram of the localization error in XYZ- and XY-space is illustrated in Fig. 3c, demonstrating a median error of 5.68 mm and 1.90 mm in the XYZ- and XY-space. As anticipated from our antenna array's geometry, the histogram for the XY distance error reveals a reduced error compared to the XYZ error distribution, related to the arrangement of the antennas in the XY plane around the head phantom, rather than stacked in the Z-direction.

The error distribution for frequency spans 0.6-1.5 GHz, 0.6-3 GHz, 0.6-6 GHz, and 0.6-9 GHz in the X-direction, Y-direction, and XY-plane are shown in Fig. 4. The PDF of the error in the X- and Y-directions and in the XY-plane both revealed squared residuals of <0.24. For the narrowest frequency span of 0.6-1.5 GHz, the distribution was the widest, achieving a maximum folded normal mean error of 2.98 mm. Conversely, the narrowest distribution (mean of 1.14 mm was obtained for the widest frequency span of 0.6-9.0 GHz). Figure 4b depicts the error distribution for the Y axis, showing that the best performance was observed for the network trained on the widest range (1.05 mm), while the least favorable performance was observed on the narrowest range (2.01 mm). Figure 4c illustrates the distance error in the XY plane; here, a similar trend was present, with the strongest performance associated with the widest frequency range of 0.6-9.0 GHz (1.65 mm). A detailed summary of the median error across frequency spans can be found in Table 1.

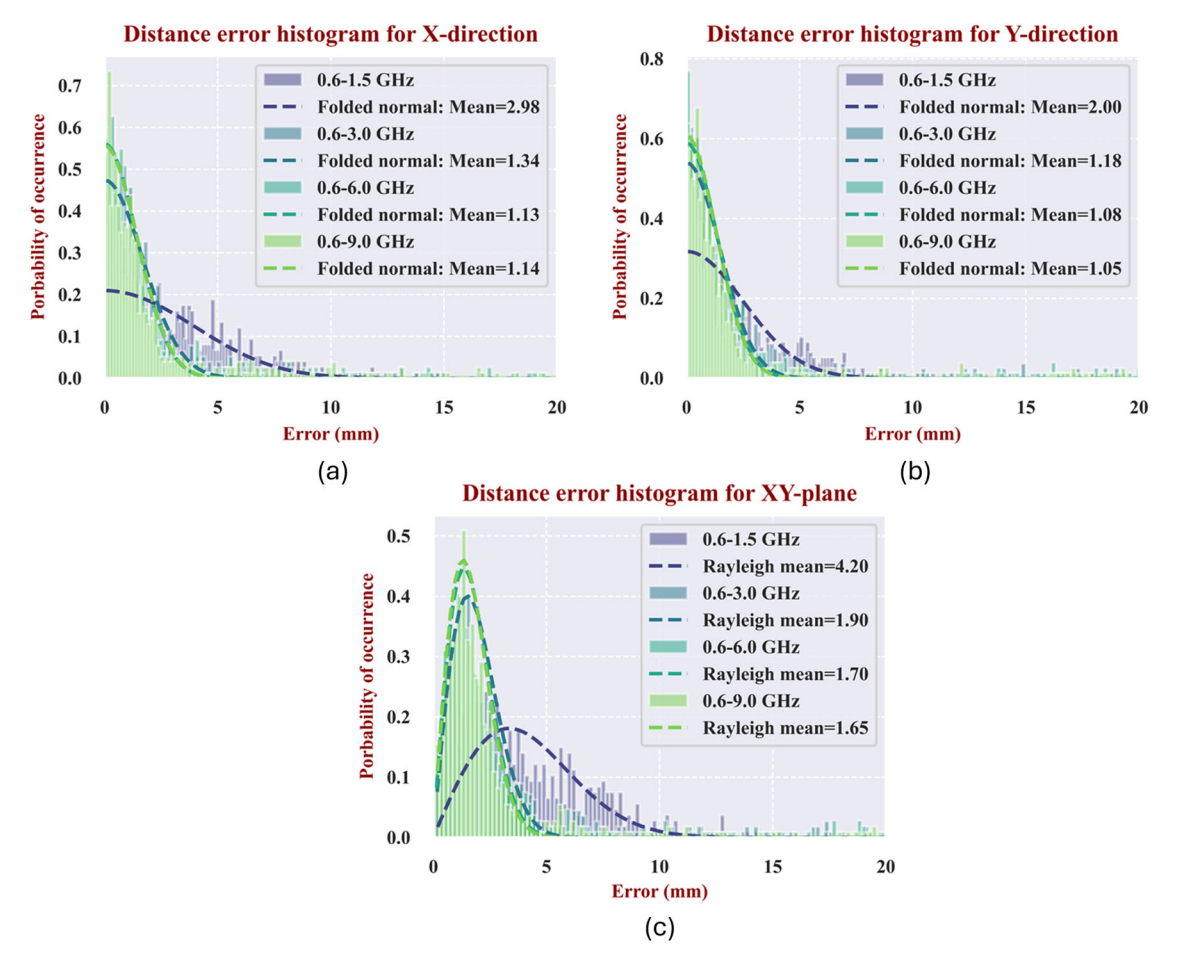


Fig. 4 | Frequency dependence of localization. Probability distribution function (PDF) of the distance error histogram for the X-direction (a), Y-direction (b), and XY-plane (c). The mean fitted Folded Normal distributions for X and Y are shown to decrease as the frequency span increases.

Fig. 5 | Antenna set and localization error.

a Placements of the antennas relative to the head phantom. b Model performance in relation to the number of antennas employed in the experiment, demonstrating the effect of increasing antenna number on localization accuracy.

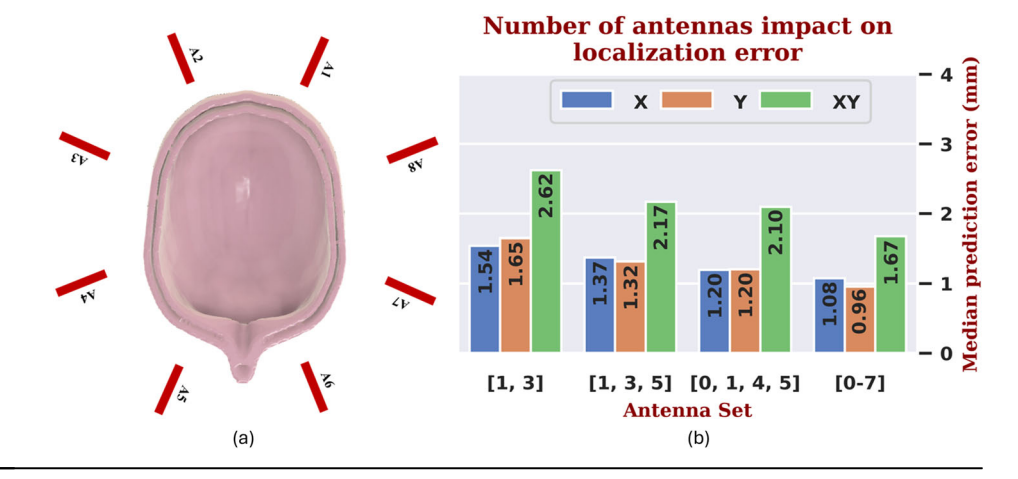


Table 2 | Median error for different antenna numbers in the array

Antenna set	Median	Median error (mm)						
	X	Υ	Z	XY	XYZ			
1 and 3	1.54	1.65	7.47	2.62	9.69			
1, 3, 5	1.37	1.32	4.85	2.17	6.37			
0, 1, 4, 5	1.20	1.20	5.62	2.10	6.96			
0–7	1.08	0.96	5.54	1.67	6.85			

The relationship between the number of antennas utilized and the stroke localization error in the X-direction, Y-direction, and XY-plane is illustrated in Fig. 5. Stroke localization error was analyzed for the full frequency span of 0.6–9.0 GHz, demonstrating a reduction of localization error as the number of antenna elements was increased. In the case of two antennas 90-degree apart (antenna 1 and 3), median localization error was 2.62 mm in the XY-direction; however, incrementally, as the number of antenna elements was increased to 8-elements, the error was reduced to 1.67 mm. With regards to the X-, Y-, and XY-directions, an increase in the error in each individual component was observed. A summary of the median error in for different antenna combinations is summarized in Table 2.

Discussion

Measurement of tissue dielectric properties has long been a focus of the biomedical community, motivated by potential applications in a multitude of neurological diseases. While past studies have reported the potential of microwave-based stroke characterization^{28,30,31,47,48}, this study utilized operating bandwidths of ~8.4 GHz and a dynamic hemorrhage model, comprising five different shapes and 127 positions.

Our system was constructed in the context of near-field stroke classification and localization, with the goal of utilizing supervised deep learning approaches to learn dielectric signatures. Because supervised learning was used to classify and localize hemorrhage models, the experimentation necessitated a flexible hemorrhage system capable of being navigated throughout the head, such that many data points could be acquired. This system included the fabrication of UWB antennas and creation of a mechanical system to mobilize blood-mimicking phantoms of varying shapes and sizes inside a multi-compartment head model. In previous in-silico reports, we have shown the potential advantages of UWB approaches for the detection of dielectric disturbances in head models³¹, and in this work, a physical realization of such a system was constructed.

A residual convolutional network structure was used as the core for higher dimensional feature extraction, and for classification and localization, a collection of fully connected layers was used. While there exist many potential approaches for learning from the complex-valued S- parameter space, our architecture was conceived as a small working model with 1.7 million parameters. In examining the classification performance more closely, a sensitivity and specificity of ~1.0 was achieved for hemorrhage detection (Fig. 3b). Further, when utilizing UWB, none of the spheres, irrespective of their size, were mistakenly predicted as star- or plus-shaped phantoms (Fig. 3a, 0.6–9.0 GHz), pointing to a remarkable sensitivity for complex morphological characteristics, even in excess of volumes alone, which were nearly identical for the disparately shaped star phantom (3.7 ml) and middle-sized sphere (3.5 ml). Similarly, predictions for the star-shaped phantom were only misclassified in any instance as a plus-shaped phantom but never as a spherical hemorrhage. The data supports that wider frequency ranges in many cases improved geometric discrimination of hemorrhages, with the most accurate classification in the 0.6-6.0 GHz sub-range.

The system yielded a median localization error for hemorrhage of 5.68 mm and 1.9 mm in the XYZ-space and XY-plane, respectively. This difference in error between the XYZ-space and XY-plane was not unexpected in view of the limited number of antennas in the Z-direction. thus limiting information in that direction. Where localization errors did occur, the effects are traceable, at least in part, to errors of the robotic system itself. Specifically, the mean XY positioning error of the robot with the attached rod was ~1.5 mm at baseline, which places in more remarkable perspective the localization accuracy of the full model. It should be noted that the best performing frequency span for the localization task was using 0.6-9.0 GHz where excellent performance in discriminating spherical and non-spherical phantoms were achieved. The results suggest that the best choice of UWB frequency ranges is likely dependent on the network architecture and the task in question. Notably, while past studies have suggested the presence of 'forbidden frequencies' between 1.5 and 4 GHz²⁹, the ablation results demonstrated the presence of valuable information encoded with these frequencies and unlocked by the neural network in use in our study. A similar conclusion was observed in our previous in-silico study, where UWB information was used for characterization and localization of hemorrhage in 2D head models31.

One limitation of this study was the dual-compartment phantom used. We have chosen this type of phantom as it allows navigation of the blood compartment within its cavity. Given that the interior of the brain-mimicking material was aqueous, this facilitated translation of the blood compartment such that scattering measurements at different positions and frequencies could be acquired in a practical timeframe and without physical or mechanical perturbation of the phantom. More anatomically realistic phantom designs would be highly desirable; nonetheless, several persistent challenges have hindered introduction of anatomically accurate phantoms, namely: (1) challenges associated with capturing the detailed anatomy of a particular subject (e.g., heads that include gray matter, white matter, CSF, muscle, etc.). (2) challenges associated with designing average anatomies from populations (i.e., obtaining the correct

average volume and structure of each compartment), and (3) challenges associated with matching the precise dielectric properties of different tissues at UWB frequencies. Such considerations act jointly towards undermining the introduction of more sophisticated and anatomically realistic head phantoms. This concession, where simpler phantoms are used has, as a result, been widely adopted by the research community and regulatory bodies (FDA, IEC, etc.) when evaluating wireless technology. Here, we aimed at creating a dynamic phantom with a moveable stroke to enable learning of hemorrhage characterization and better understand the utilization of UWB together with machine learning for the task. The goal was motivated by previous in-silico and in-vivo studies by our group and others, suggesting that machine learning algorithms can be used to characterize the size and location of hemorrhage 31,39,62,63. Such machine learning approaches often require large datasets, and thus we aimed to demonstrate that large datasets can be created with this type of dynamic phantom and UWB microwave setup.

While the anatomic complexity of the human head exceeds that attainable in physical phantoms, this carries the associated benefits of greater dielectric complexity and greater variations in the dielectric properties across the frequencies tested, and hence the potential for greater discrimination between the signatures of normal and pathologic tissues. These greater dielectric differences at different frequencies can assist learning to identify and characterize stroke with suitable algorithms. Furthermore, while many hemorrhages may be ovoid by nature, in this study, two more complex hemorrhage shapes (cross and star) were included. The goal of including these shapes was to introduce more subtle dielectric structures to differentiate between, resulting in a differentiation accuracy of ~85%, when scanning from 0.6 to 9 GHz. Notwithstanding, even though highly desirable, the introduction of more complex phantoms into this framework, requires further research in terms of the phantom design (while allowing a dynamic stroke to be placed inside the phantom) and preparation of dielectric fluids that closely resemble the anatomy at UWB frequencies. These tasks are unfortunately beyond the scope of this work and would need to be investigated in future studies.

It should be noted that acquisitions were conducted on muscle-brain, air- and water-filled mediums. These scans were conducted over the course of many weeks, since for each condition many positions were measured, and each measurement was performed only after the liquid system was allowed to stabilize. This required a highly controlled environment during the experiments and as a result measurements were conducted on a single head phantom. Experiments on more phantoms would result in a linear increase in measurement time with the number of additional phantoms while most likely resulting in better generalization across phantoms. Future research may include an investigation of the reduction of scan time to accommodate experimentation on a greater number of phantoms. With regards to the stroke classification problem, we designed the study such that stroke can be classified similar to many other supervised learning classification studies (e.g., supervised approaches to classify animals from photos, where different instances of all the classes are fed into the model for training). In this context, future studies may include a model that can estimate the geometry of the stroke based on the scattering information alone, similar to back-scattering reconstructions that are often used in microwave imaging. Overall, the performance of our system benefitted from several unique attributes, including the successful development of UWB capabilities spanning 0.6-9.0 GHz.

Conclusion

This work reports, for the first time, the benefits of localization accuracy enabled through the use UWB hardware alongside deep neural network, as well as hemorrhage classification with dynamic phantoms. The apparent sensitivity to morphologic characteristics, in excess of simple dimensional or volumetric features, points strongly to the benefits of deep learning tools in the exploration of UWB microwave scattering. The overarching longitudinal goal of this study was to establish practical foundations of operation and to lay the physical groundwork prior to human scanning. Among the

practical outcomes of the current study was the design of the acquisition system, UWB antennas, and other hardware that are directly translatable towards UWB scanning of humans. Furthermore, the initial convolutional neural nets defined here (with possible modification) can be used once moving to future subject scanning. In future work on stroke patients, stroke localization and characterization can be possible by learning diagnoses from the radiologic imaging which will be used for training the neural net from the UWB measurements (as inputs). Therefore, we view this work as a steppingstone for better understanding the impact of UWB as a potentially clinically translatable tool. Among the benefits of a fully realized UWB scanning system is the ability to collect vast amounts of scattering data with an acquisition speed far exceeding conventional MRI protocols, and at a far lower cost for deployment compared to gold-standard imaging systems. We thus foresee the possibility for relatively seamless introduction of future clinical systems that could be trained and tuned against ground truth human subjects imaging to extend the observations of our benchtop model to the clinical domain.

Data availability

S-parameters data for the air-, water-, and muscle- brain-filled phantoms and all positions can be downloaded in reference⁶⁴. Where, for each phantom condition all measurement positions were saved to a single HDF5 (h5) binary data file.

Code availability

Reconstruction code utilized for non-commercial use can be found in reference⁶⁴, under the "code" directory.

Received: 2 January 2024; Accepted: 5 August 2024; Published online: 05 September 2024

References

- World Stroke Organization. What We Do. https://www.world-stroke. org/what-we-do (2024).
- Addo, J. et al. Socioeconomic status and stroke. Stroke 43, 1186–1191 (2012).
- Benjamin, E. J. et al. Heart disease and stroke statistics—2019 update: a report from the American Heart Association. *Circulation* 139, e56–e528 (2019).
- 4. Saver, J. L. Time is brain-quantified. Stroke 37, 263-266 (2006).
- Wintermark, M. et al. Acute stroke imaging research roadmap. Stroke 39, 1621–1628 (2008).
- Fisher, M. Characterizing the target of acute stroke therapy. Stroke 28, 866–872 (1997).
- Yaghi, S., Bianchi, N., Amole, A. & Hinduja, A. ASPECTS is a predictor of favorable CT perfusion in acute ischemic stroke. *J. Neuroradiol* 41, 184–187 (2014).
- Kane, I. et al. Comparison of 10 different magnetic resonance perfusion imaging processing methods in acute ischemic stroke: effect on lesion size, proportion of patients with diffusion/perfusion mismatch, clinical scores, and radiologic outcomes. Stroke 38, 3158–3164 (2007).
- Heiss, W. D. The ischemic penumbra: correlates in imaging and implications for treatment of ischemic stroke. The Johann Jacob Wepfer Award 2011. Cerebrovasc. Dis. 32, 307–320 (2011).
- Krieger, D. A. & Dehkharghani, S. Magnetic Resonance Imaging in Ischemic Stroke and Cerebral Venous Thrombosis. *Top. Magn. Reson. Imaging* 24, 331–352 (2015).
- Dehkharghani, S. et al. Performance of CT ASPECTS and Collateral Score in Risk Stratification: Can Target Perfusion Profiles Be Predicted without Perfusion Imaging?. AJNR Am. J. Neuroradiol. 37, 1399–1404 (2016).
- Dehkharghani, S. et al. Performance and predictive value of a userindependent platform for CT perfusion analysis: threshold-derived automated systems outperform examiner-driven approaches in

- outcome prediction of acute ischemic stroke. *AJNR Am. J. Neuroradiol.* **36**, 1419–1425 (2015).
- Dehkharghani, S. & Andre, J. Imaging approaches to stroke and neurovascular disease. Neurosurgery 80, 991 (2017).
- Wintermark, M. et al. Comparison of CT perfusion and angiography and MRI in selecting stroke patients for acute treatment. *Neurology* 68, 694–697 (2007).
- Bao, D. Z. et al. 64-Slice spiral CT perfusion combined with vascular imaging of acute ischemic stroke for assessment of infarct core and penumbra. Exp. Ther. Med. 6, 133–139 (2013).
- Kucinski, T. et al. Cerebral perfusion impairment correlates with the decrease of CT density in acute ischaemic stroke. *Neuroradiology* 46, 716–722 (2004).
- Walter, S. et al. Diagnosis and treatment of patients with stroke in a mobile stroke unit versus in hospital: a randomized controlled trial. *Lancet Neurol.* 11, 397–404 (2012).
- Greenberg, S. M. et al. 2022 Guideline for the management of patients with spontaneous intracerebral hemorrhage: a guideline from the American Heart Association/American Stroke Association. Stroke 53, e282–e361 (2022).
- Wald, L. L., McDaniel, P. C., Witzel, T., Stockmann, J. P. & Cooley, C. Z. Low-cost and portable MRI. J. Magn. Reson. Imaging 52, 686–696 (2020).
- World Health Organization. Essential Diagnostic Imaging Report. https://web.archive.org/web/20121023154427/ https://www.who.int/eht/en/DiagnosticImaging.pdf (2012).
- Fransen, P. S. S. et al. Time to reperfusion and treatment effect for acute ischemic stroke: a randomized clinical trial. *JAMA Neurol.* 73, 190–196 (2016).
- Dehkharghani, S. et al. High-performance automated anterior circulation CT angiographic clot detection in acute stroke: a multireader comparison. *Radiology* 298, 665–670 (2021).
- Heit, J. J. et al. Automated cerebral hemorrhage detection using RAPID. Am. J. Neuroradiol. 42, 273 (2021).
- John, S. et al. Brain imaging using mobile CT: current status and future prospects. J. Neuroimag. 26, 5–15 (2016).
- Fassbender, K. et al. "Mobile stroke unit" for hyperacute stroke treatment. Stroke 34, e44 (2003).
- Ebinger, M. et al. Effect of the use of ambulance-based thrombolysis on time to thrombolysis in acute ischemic stroke: a randomized clinical trial. *JAMA* 311, 1622–1631 (2014).
- Walter, S. et al. Mobile stroke units-cost-effective or just an expensive hype? Curr. Athero. Scler. Rep. 20, 1–6 (2018).
- Semenov, S. Y. et al. Microwave-tomographic imaging of the high dielectric-contrast objects using different image-reconstruction approaches. *IEEE Trans. Microw. Theory Tech.* 53, 2284–2294 (2005).
- Scapaticci, R., Di Donato, L., Catapano, I. & Crocco, L. "A feasibility study on microwave imaging for brain stroke monitoring,". *Prog. Electromagn. Res. B* 40, 305–324 (2012).
- Guo, L., Alqadami, A. S. M. & Abbosh, A. Stroke diagnosis using microwave techniques: review of systems and algorithms. *IEEE J. Electromagn. RF Microw. Med. Biol.* 7, 122–135 (2023).
- Alon, L. & Dehkharghani, S. A stroke detection and discrimination framework using broadband microwave scattering on stochastic models with deep learning. Sci. Rep. 11, 24222 (2021).
- Hagness, S. C., Taflove, A. & Bridges, J. E. Two-dimensional FDTD analysis of a pulsed microwave confocal system for breast cancer detection: fixed-focus and antenna-array sensors. *IEEE Trans. Biomed. Eng.* 45, 1470–1479 (1998).
- Popovic, D. et al. Precision open-ended coaxial probes for in vivo and ex vivo dielectric spectroscopy of biological tissues at microwave frequencies. *IEEE Trans. Microw. Theory. Tech.* 53, 1713–1722 (2005).
- Lazebnik, M. et al. A large-scale study of the ultrawideband microwave dielectric properties of normal, benign and malignant

- breast tissues obtained from cancer surgeries. *Phys. Med. Biol.* **52**, 6093 (2007).
- Fear, E. C., Li, X., Hagness, S. C. & Stuchly, M. A. Confocal microwave imaging for breast cancer detection: localization of tumors in three dimensions. *IEEE Trans. Biomed. Eng.* 49, 812–822 (2002).
- O'Halloran, M., Glavin, M. & Jones, E. Rotating antenna microwave imaging system for breast cancer detection. Progress in electromagnetics. *Research* 107, 203–217 (2010).
- 37. Xie, Y., Guo, B., Xu, L., Li, J. & Stoica, P. Multistatic adaptive microwave imaging for early breast cancer detection. *IEEE Trans. Biomed. Eng.* **53**, 1647–1657 (2006).
- 38. Vasquez, J. A. T. et al. A prototype microwave system for 3d brain stroke imaging. *Sensors* **20**, 2607 (2020).
- Abbosh, A. et al. Clinical electromagnetic brain scanner. Sci. Rep. 14, 5760 (2024).
- Medfield Diagnostics. Microwave Technology For Faster Diagnosis. https://www.medfielddiagnostics.com/technology/ (2024).
- 41. UBT SRL Italy. *MammoWave: a New Device for Breast Lesion Detection*. https://www.ubt-tech.com/ (2024).
- 42. Woods, D. Multiport-network analysis by matrix renormalization employing voltage-wave S-parameters with complex normalization. *Proc. Inst. Electr. Eng.* **124**, 198–204 (1977).
- Meaney, P. et al. A 4-channel, vector network analyzer microwave imaging prototype based on software defined radio technology. Rev. Sci. Instrum. 90, 044708 (2019).
- Hurt, W. D. Radio Frequency Radiation Dosimetry Workshop: Present Status and Recommendations for Future Research. Defense Technical Information Center. https://apps.dtic.mil/sti/tr/pdf/ADA309928.pdf (1996).
- 45. Dority, J. S. & Oldham, J. S. Subarachnoid hemorrhage: an update. Anesthesiol. Clin. **34**, 577–600 (2016).
- Kostanian, V., Choi, J. C., Liker, M. A., Go, J. L. & Zee, C. S. Computed tomographic characteristics of chronic subdural hematomas. *Neurosurg. Clin. N Am.* 11, 479–489 (2000).
- 47. Al-Saffar, A. et al. Closing the gap of simulation to reality in electromagnetic imaging of brain strokes via deep neural networks. *IEEE Trans. Comput. Imaging.* **7**, 13–21 (2021).
- Candefjord, S. et al. Microwave technology for detecting traumatic intracranial bleedings: tests on phantom of subdural hematoma and numerical simulations. *Med. Biol. Eng. Comput.* 55, 1177–1188 (2017).
- Siddiqui, J. Y. et al. Design of an ultrawideband antipodal tapered slot antenna using elliptical strip conductors. *IEEE Antennas Wirel. Propag. Lett.* 10, 251–254 (2011).
- Kainz, W. et al. Dosimetric comparison of the specific anthropomorphic mannequin (SAM) to 14 anatomical head models using a novel definition for the mobile phone positioning. *Phys. Med. Biol.* 50, 3423–3445 (2005).
- SCRIBD. Ned User Manual v3.1.1 Documentation. https://docs.niryo.com/product/ned/v3.1.1/en/source/introduction.html#robot (2024).
- Steeman, P. A. M., Maurer, F. H. J. & Van Turnhout, J. Dielectric properties of blends of polycarbonate and acrylonitrile-butadienestyrene copolymer. *Polym. Eng. Sci.* 34, 697–706 (1994).
- 53. Ferrero, A. & Pisani, U. Two-port network analyzer calibration using an unknown 'thru'. *IEEE Microw. Guid. Wave Lett.* **2**, 505 (1992).
- Williams, D. F. & Walker, D. K. In-line multiport calibration. 51st ARFTG conference digest-spring: characterization of spread spectrum telecommunications components and systems. ARFTG 1998, 88–90 (1998).
- Martens, J., Judge, D. & Bigelow, J. VNA Calibration Modifications and Hybridizations for Simplified High Frequency Multiport/Differential Measurements. https://www.armms.org/media/uploads/ 1128506761.pdf (2005).
- Arsenovic, A. et al. scikit-rf: An open source python package for microwave network creation, analysis, and calibration [Speaker's Corner]. *IEEE Microw. Mag.* 23, 98–105 (2022).

- He, K., Zhang, X., Ren, S. & Sun, J. Deep residual learning for image recognition. *IEEE Conf. Computer Vision and Pattern Recognition* (CVPR). 770–778 (IEEE, Las Vegas, 2016).
- Kingma, D. P. & Ba, J. Adam: A method for stochastic optimization. arXiv. preprint arXiv, 1412.6980 (2014).
- Leone, F. C., Nelson, L. S. & Nottingham, R. B. The folded normal distribution. *Technometrics* 3, 543–550 (1961).
- Beckmann, P. Rayleigh distribution and its generalizations. Radio science. J. Res. NBS/USNC-URSI 68, 927–932 (1964).
- 61. Virtanen, P. et al. SciPy 1.0: fundamental algorithms for scientific computing in python. *Nat. Methods* **17**, 261–272 (2020).
- Lai, W. C., Guo, L., Bialkowski, K. & Bialkowski, A. An explainable deep learning method for microwave head stroke localization. *IEEE J. Electromagn. RF Microw. Med. Biol.* 7, 336–343 (2023).
- Gabriel, C., Gabriel, S. & Corthout, E. The dielectric properties of biological tissues: I. Literature survey. *Phys. Med. Biol.* 41, 2231–2249 (1996 Nov).
- 64. Hedayati E. Code for Processing and Reconstruction of Microwave Information. https://www.dropbox.com/scl/fo/rv7g75gywzvuwfr6b4p7b/ALwHoWn2nHAO3pZPW9zvB0E?rlkey=oj0r6lut7tjgj96apzk14wrsz&dl=0 (2024).

Acknowledgements

This work was supported in part by NIH grant P41-EB017183.

Author contributions

S.D. and L.A. conceived the idea and proposed the project. F.S. designed the microwave antennas. E.H., F.S., and G.V. designed the robotic setup. E.H., V.R.C., F.S., and L.A. helped design the 3D phantom setup. F.S. and G.V. assisted in the electronics setup construction. F.S. conducted the experiments necessary to develop the dielectric liquids for phantom creation. E.H. and F.S. conducted the experiments and were responsible for data acquisition. E.H. developed the data acquisition framework software, built the Al powered machine learning method, and was responsible for evaluation and interpretation of the results. D.K.S. assisted in the experimental design and manuscript preparation. Manuscript writing was conducted by S.D., E.H., and L.A. and revised by all authors.

Competing interests

The authors S.D and L.A declare the existence of a non-financial competing interest in the form of intellectual property (US patent US20210335493A1,

entitled: "System to detect dielectric changes in matter"), which describes microwave methods used for detection of dielectric changes.

Additional information

Supplementary information The online version contains supplementary material available at https://doi.org/10.1038/s44172-024-00259-4.

Correspondence and requests for materials should be addressed to Seena Dehkharghani or Leeor Alon.

Peer review information Communications Engineering thanks the anonymous reviewers for their contribution to the peer review of this work. Primary Handling Editors: Anastasiia Vasylchenkova and Rosamund Daw. A peer review file is available.

Reprints and permissions information is available at http://www.nature.com/reprints

Publisher's note Springer Nature remains neutral with regard to jurisdictional claims in published maps and institutional affiliations.

Open Access This article is licensed under a Creative Commons Attribution-NonCommercial-NoDerivatives 4.0 International License, which permits any non-commercial use, sharing, distribution and reproduction in any medium or format, as long as you give appropriate credit to the original author(s) and the source, provide a link to the Creative Commons licence, and indicate if you modified the licensed material. You do not have permission under this licence to share adapted material derived from this article or parts of it. The images or other third party material in this article are included in the article's Creative Commons licence, unless indicated otherwise in a credit line to the material. If material is not included in the article's Creative Commons licence and your intended use is not permitted by statutory regulation or exceeds the permitted use, you will need to obtain permission directly from the copyright holder. To view a copy of this licence, visit http://creativecommons.org/licenses/by-nc-nd/4.0/.

© The Author(s) 2024